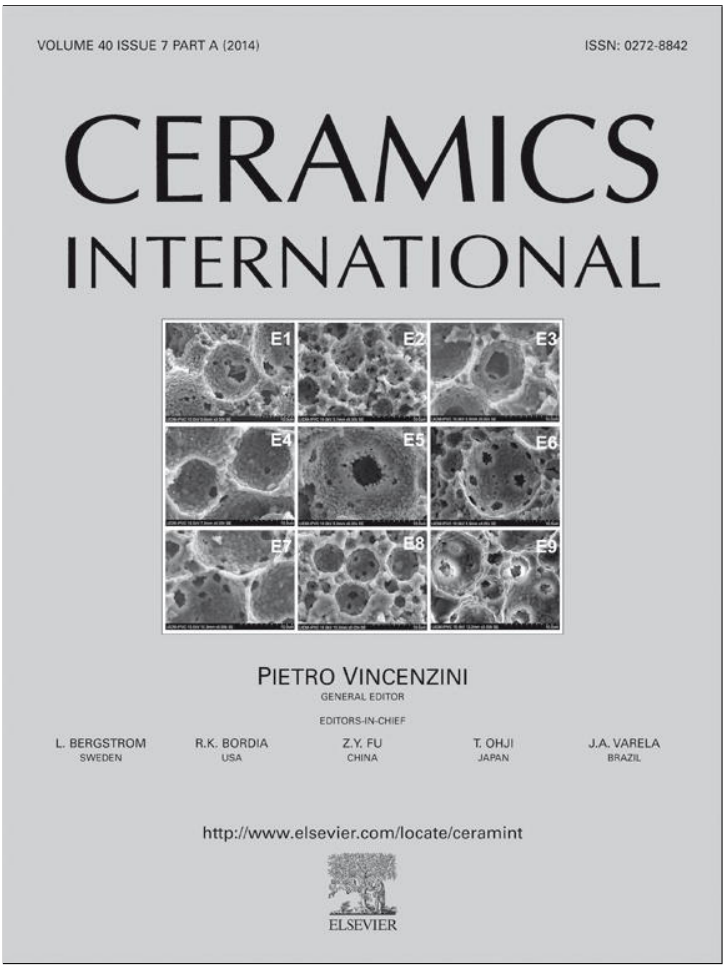

Available online at www.sciencedirect.com

ScienceDirect

Ceramics International 40 (2014) 9133–9149

CERAMICS INTERNATIONAL

www.elsevier.com/locate/ceramint

Physical, chemical and thermal characterization of alumina–magnesia–carbon refractories

Vanesa Muñoz[a], Pilar Pena[b], Analía Gladys Tomba Martínez[a,*]

[a]*Instituto de Investigaciones en Ciencia y Tecnología de Materiales (INTEMA), CONICET-Facultad de Ingeniería, Universidad Nacional de Mar del Plata, Av. J.B. Justo 4302, 7600 Mar del Plata, Argentina*

[b]*Instituto de Cerámica y Vidrio (ICV), CSIC, Kelsen 5, 28049 Madrid, Spain*

Received 29 October 2013; received in revised form 23 January 2014; accepted 28 January 2014
Available online 17 February 2014

Abstract

Alumina–magnesia–carbon refractories (AMC) are of great technological interest for their use as linings for iron and steelmaking ladles. In this paper, the methodology implemented for the physical, chemical and thermal characterization of AMC refractories is presented along with the obtained results. These results are essential for the study of the chemical and mechanical behavior of these materials, which the present work frames. AMC bricks comprise different amounts of alumina, sintered or electrofused magnesia, graphite and antioxidant additives bonded together with a phenolic resin. The variety of components, be they oxidic, metallic or polymeric in nature, and the complexity of the final microstructure and texture make characterizing these refractories a difficult task. In the present work, several complementary techniques were used in combination: X-ray fluorescence, plasma emission spectroscopy, gravimetry, X-ray diffraction, differential thermal and thermogrametric analyses, reflection optical microscopy and scanning electron microscopy, density and porosity measurements, dilatometric analysis and permanent linear change measurements. The results of these different techniques were analyzed separately and together in order to obtain a detailed description of each refractory in relation to its physical and chemical characteristics and thermal evolution. In addition, the characterization was completed by evaluating the mechanical properties at room temperature, such as the mechanical strength and Young's modulus.

Keywords: B. Microstructure-final; C. Mechanical properties; D. Al_2O_3, MgO, carbon; E. Refractories

1. Introduction

Alumina–magnesia–carbon refractories (AMC) appeared in the 1980s as a solution to the drawbacks in performance shown by the linings of steelmaking ladles made of Al_2O_3–C bricks on one hand and MgO–C bricks on the other [1]. The excellent performance of AMC materials is due to the combination of high refractory oxides such as corundum (α-Al_2O_3) and periclase (MgO) with graphite (C). The oxidic components are highly resistant to mechanical loading, erosion and abrasion and moderately resistant to chemical attack by melts. The presence of graphite enhances refractory performance in several ways: (a) since it is not wetted by metals or slags, graphite prevents these liquids from penetrating through open pores, thus reducing chemical wear; (b) the low thermal expansion and high thermal conductivity of graphite increase the thermal shock resistance of the brick; and (c) graphite provides flexibility to the structure due to its ability to absorb thermal and/or mechanical stresses.

However, graphite oxidizes easily at high temperature, and this process could determine the behavior of these materials in service, particularly in the case of an open vessel such as a ladle. In order to increase their resistance to graphite oxidation, a controlled amount of antioxidants are added to these materials, the most common of which are metals and metallic alloys and, less frequently, carbides and borides. In service, these additives react with C and the gases inside the pores

*Corresponding author. Tel.: +54 223 4816600; fax: +54 223 4810046.
E-mail address: agtomba@fi.mdp.edu.ar (A.G.T. Martínez).

http://dx.doi.org/10.1016/j.ceramint.2014.01.128
0272-8842

(O_2, CO and/or N_2) forming other compounds (carbides, oxides and nitrides); these reactions help prevent graphite loss by oxidation. The new compounds crystallize as plates or whiskers, which fill the pores and/or react with ceramic particles (alumina or magnesia) to form other solid phases. Both these processes also enhance the mechanical and chemical properties of the brick.

Besides the heterogeneous nature of their inorganic, organic and metallic components, AMC refractories comprise particles with a wide granulometric range, including coarse (1–6 mm), medium (1 mm–120 μm) and fine (< 120 μm) fractions. The oxidic components—alumina (tabular, electrofused and/or bauxite) and magnesia (sintered and/or electrofused) aggregates—are distributed in the medium and coarse fractions. The fine fraction, which is the matrix, is more heterogeneous and is formed by the same oxidic particles, graphite flakes (between 5 and 15 wt% [2]) and, in general, aluminum as an antioxidant ($\sim$2–3 wt%). The total amount of MgO varies between 2 and 35 wt% [2,3]. The bonding between the inorganic particles is performed at room temperature using polymeric organic binders, usually phenolic resins ($\sim$2–3.5 wt% [2]) such as novolaka or resol, which are cured in the range of 100–300 °C.

At high temperature, alumina, magnesia and the aluminum present in the fine fraction of AMC type refractories, react according to several mechanisms leading to the formation of spinel ($MgAl_2O_4$) *in situ* (due to these reactions, these refractories are referred to as 'alive' or 'mutant' materials). This spinelization is accompanied by volumetric expansion ($\sim$8% when magnesia reacts with alumina) that counteracts the bricks' joint wear [1,3–7]. In addition, this expansion also induces microcracking due to differences between the thermal expansions of the reagents and the products, which could give rise to toughening mechanisms; however, these microcracks may also become points where chemically aggressive agents could enter into the brick. For these reasons, the reactions that cause spinel formation have to be controlled, which signifies that the MgO content has to be optimized.

The behavior of AMC refractories under mechanical, thermal and thermomechanical loadings and also their chemical behavior are directly related to the raw materials' composition, granulometry, purity and contents. All these factors determine the final microstructure and texture of the brick. The study of commercial refractories, which is quite uncommon due to the impossibility of controlling the chemical composition and/or the microstructure of the brick, does however have the advantage of avoiding the problems linked to reproducing the manufacturing process at a laboratory scale, which is not a trivial issue due to the low affinity between the main refractory components. Moreover, the results can be applied directly to the material's performance in the plant. However, the study of commercial bricks imposes the necessity of characterizing them in a comprehensive manner, particularly if the understanding of their behavior is to be based on relationships between their composition, microstructure and properties. By using several complementary analytical–chemical, mineralogical, microstructural, textural and thermal techniques, it is possible to obtain data that can be used to generate a detailed description of the material. For materials with such a high heterogeneity, *ad-hoc* methodologies are needed to obtain reliable information for certain aspects. For other aspects, however, no characterization technique has yet been developed.

Similar to other published papers dealing with the analytical characterization of MgO–C [8] and Al_2O_3–MgO–C [9] refractories, the aim of the this research is to establish a methodology for the comprehensive analysis of AMC-type commercial refractories while including other aspects besides their chemical and mineralogical composition, such as their microstructure, texture, thermal behavior and typical mechanical properties at room temperature. This methodology was applied to three commercial AMC refractories used to line the walls and bottoms of steelmaking ladles that come in contact with the melted metal. Analyzing these selected aspects required the use of several techniques, most of which are not standard for these types of materials. In addition, they were selected taking into account the experimental simplicity involved and the accuracy of the data obtained from them. The experimental data were then used in basic studies of the mechanical behavior and slag-corrosion resistance of these types of refractories, which will be the subject of future publications.

2. Experimental procedure

2.1. Materials

Three commercial Al_2O_3–MgO–C bricks used to line the walls and bottoms of ladles in a local steel shop were analyzed. They were made by the same manufacturer and labeled as AMC1, AMC2 and AMC3. According to the technical data sheets, these refractories were formulated with different proportions of alumina tabular aggregates and/or bauxite, sintered magnesia, graphite and an antioxidant and bonded with resin.

2.2. Methodology

The methodology established for characterizing the AMC commercial bricks includes those aspects considered as determining the performance of these materials in service, which is also related to their behavior under thermal and mechanical loads and/or chemically aggressive conditions. Several combined techniques were selected taking into account the experimental simplicity, the reliability of data as well as the heterogeneity of the studied materials. The aspects and the analytical techniques used to characterize them are listed below.

a) *Microstructure*: Reflected light optical microscopy and scanning electron microscopy coupled with X-ray energy dispersive spectroscopy (SEM/EDS) were used; the nature of raw materials used to prepare the bricks and their distribution in the granulometric fractions were among the aspects evaluated. The estimation of particle sizes larger

than 0.1 mm (the smallest size that can be distinguished with the magnification used), which fall within the coarse- and medium-sized granulometric fractions, was also performed.

b) *Mineralogical composition*: Determined by qualitative X-ray diffraction (XRD) together with observations made by reflected light optical microscopy and scanning electron microscopy coupled with X-ray dispersive energy (SEM/EDS). The quantification of the main components was carried out by the rational analysis of the chemical analysis data, as was previously reported [9].

c) *Chemical composition*: An *ad-hoc* methodology described in a previous paper by the authors [9] was used that combines X-ray fluorescence (XRF), plasma emission spectroscopy (ICP-OES) and gravimetry to analyze powdered samples previously treated with specific thermal schedules.

d) *Texture*: Several complementary techniques, such as measurements of global and picnometric densities, total, open and closed porosities and permeability were used to characterize the pores. A standardized methodology [10] could be used as a reference only with the techniques for determining densities and porosities. Pores sizes were estimated by mercury intrusion porosimetry.

e) *Thermal evolution of phases*: The characteristic changes occurring in these materials with the increase of temperature were determined by differential thermal and thermogravimetric analyses (DTA/TGA) under oxidant atmosphere (air). Specific thermal treatments were carried out on brick fragments in order to take into account the effect of texture. Finally, mineralogical qualitative analysis by XRD was performed on powdered samples obtained from the treated bodies. The results of this study were reported in a paper previously published by the authors [11].

f) *Dimensional change*: Since the residual expansion of these materials is one of their positive aspects, the dimensional change of the bricks with respect to temperature was evaluated by dilatometric analysis and measurements of the permanent linear change (PLC) in air.

g) *Mechanical properties at room temperature*: These properties are not indicative of the performance of the bricks in service because they are strongly affected by temperature; however, these values help to further characterize these refractories. An alternative test for obtaining stress–strain curves that gives additional information on the material's mechanical behavior was used [12] even though standards for determining mechanical parameters of carbon-containing refractories are available [13]. Conventional properties such as Young's modulus and mechanical strength along with others less frequently measured such as fracture strain and yield stress were determined.

2.2.1. Samples and specimens preparation

Powdered samples and specimens representative of the unused original bricks were used for the analysis of AMC refractories.

The powdered samples were prepared from fragments ($\sim$200 g) cut from the original bricks. Firstly, a coarse grinding was performed (manually) up to a granulometry suitable for manipulation (<1 cm). Then, a finer grinding was carried out in a planetary mill (Planetary – Micro Mill "Pulverisette 7" Fritsch) at 595 rpm for intervals of 5 min until the particle size required for each of the analytical techniques was obtained (between 75 and 120 μm). For the hardest components corresponding to the different alumina aggregates, a manual grinding using an impact mortar of tungsten carbide was necessary. When the sample was completely reduced to the required particle size, it was successively quartered.

The specimens used in the different tests were (a) cylinders 27–46 mm in diameter and 20–40 mm in height for global density, apparent porosity and permeability measurements, microstructural analysis and mechanical tests and (b) prismatic specimens $30 \times 30 \times 50$ mm^3 with a square cross-section, for dilatometry and PLC measurements. The ASTM C133-94 [14] recommendations for mechanical testing were followed for selecting the specimen's dimensions. These recommendations specify that the smallest dimension of the specimen must be at least 4 times larger than the largest aggregate. The specimens were cut from the original bricks using diamond-cutting disks and diamond drills for case (a) and by cutting only for case (b). In both cases, water was used for cooling.

The specimens were impregnated in polyester or epoxy resins in a vacuum in order to observe their surfaces (microstructural analysis by microscopy). Then, the surfaces were sequentially ground with 320, 600, 1200 and 4000 grit SiC paper, with kerosene used as a lubricant. For the final polishing, diamond pastes up to 1 μm were used.

2.2.2. Experimental techniques

The reflected light optical microscopy was carried out on polished surfaces using Zeiss Axiophot equipment. For the microstructural analysis by SEM/EDS, both Philips XL30 and Joel JSM-6460 microscopes were used.

Particle sizes larger than 0.1 mm (including oxidic coarse aggregates and particles of the medium-sized fraction) were estimated from photographs ($4\times$ magnification) of the polished surfaces (≈ 6 cm^2) using Image Pro Plus 6.0 software and counting between 120 and 300 particles. The mean diameter of each particle (D) was obtained as the average length of the diameters measured at intervals of 5°, taking the centroid of each particle as its center. The size of aluminum and graphite particles (both type of particles included in the matrix) were estimated by analyzing optical microscopy images using the software mentioned previously and counting between 80 and 120 particles for the metallic additive and between 18 and 25 for the graphite flakes. In the latter case, the length (L) and the thickness (A) of each particle were measured, and for aluminum, the mean diameter D was determined in the same manner as with the oxide particles. The maxima (D_{max}, L_{max}, A_{max}) and minima (D_{min}, L_{min}, A_{min}) values of each distribution as well as those corresponding to a cumulative percentage of 50% in number (D_{50}, L_{50}, A_{50}) were considered as statistical parameters.

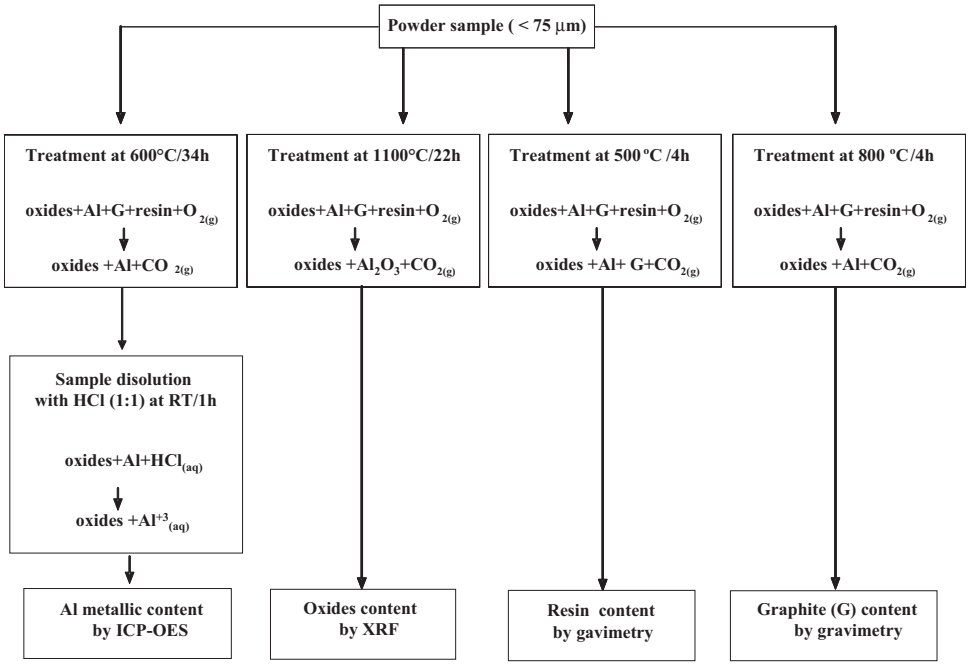

Fig. 1. Diagram of the *ad-hoc* method for chemical analysis of AMC refractories.

The XRD analysis was performed on powdered simples < 75 μm in a Brucker Advanced DV8 diffractometer, using Cu Kα radiation (1.5418 Å), primary monocromator Kα1, with a voltage of 40 kV and 40 mA of current, and a multichannel detector ('lynx eye'). The angular interval used was 20–70° 2θ, with a step of 0.099° and an acquisition time of 229.5 s per step.

For the chemical analysis of AMC refractories, an *ad-hoc* methodology was used that was developed and described in a paper published previously by the authors [9]. In Fig. 1, a diagram of the experimental procedure is shown. A PANalytical, MagicX (PW-2424) spectrometer with an Rh anode X-ray tube (Super Sharp) and 2.4 kW generator was used, equipped with analytic software (IQ^+) for qualitative and semi-quantitative analysis based on the interelemental correction from fundamental parameters. The technique was applied on powdered samples treated at 1100 °C (to eliminate the resin and graphite and oxidize the aluminum) and prepared in the form of pearls by melting with $Li_2B_4O_7$ at 1050 °C using a Perl'X3, Philips equipment and a Pt-Au crucible. To quantify the metallic aluminum by ICP-OES, Thermo Jarrell Ash IRIS Advantage Axial Plasma equipment was used with a radio-frequency generator of 40.68 MHz and solid state CIF (Charge Injection Device) detector. The Al was previously separated from a powdered sample (< 75 μm) treated at 600 °C (for resin and graphite elimination) by acid attack with HCl. Resin and graphite contents were obtained by measuring the weight loss in the powdered samples after treatments at 500 and 800 °C, respectively, in order to selectively eliminate each of these components [9]. A Sartorius BP 221 S9 analytical balance was used for this purpose.

The rational analysis of chemical composition data, together with information resulting from the mineralogical and microstructural analyses, enables the present phases to be quantified [9]. Taking into account the experimental error (± 5 wt%) and the complexity associated with the Rietveld method, which is commonly used in quantitative analysis by XRD, the rational analysis turns out to be a more simple, practical and accurate technique.

The global density (ρ_g) and the apparent porosity (π_a) of AMC refractories were determined in duplicate on cylinders 27 mm in diameter and 40 mm in height, based on the DIN 51056 standard [10]. A Sartorius BP 221 S analytical balance and kerosene (as the fluid of known density) were used. The solid density (ρ_{pic}) was determined by helium picnometry using a Multipycnometer, Quantachrome Co. equipment and ~25–30 g of powder < 210 μm. The true porosity (π_v) and the close porosity (π_c) were calculated using the following equations:

$$\pi v = \frac{(\rho pic - \rho g) \times 100}{\rho pic}$$

$$\pi_c = \pi_v - \pi_a$$

Mercury intrusion porosimetry was used to analyze the pore size distributions. This was done with AutoPore II 9215, Micromeritics (USA) equipment and fragments of bricks with a volume of $\approx 2.5\ cm^3$. To obtain the permeability of the refractory bricks, an in-house-designed and constructed apparatus based on the gas flow through the specimen and pressure difference between the incoming and outgoing gas was utilized. A nitrogen flow and disks 46 mm in diameter and 20 mm in height were used.

The thermal differential and thermogravimetric analyses of materials were carried out up to 1400 °C on powdered samples < 75 μm (13–19 mg) using Shimadzu DTA-50 and TGA-50 equipment respectively. Each run was performed with an air

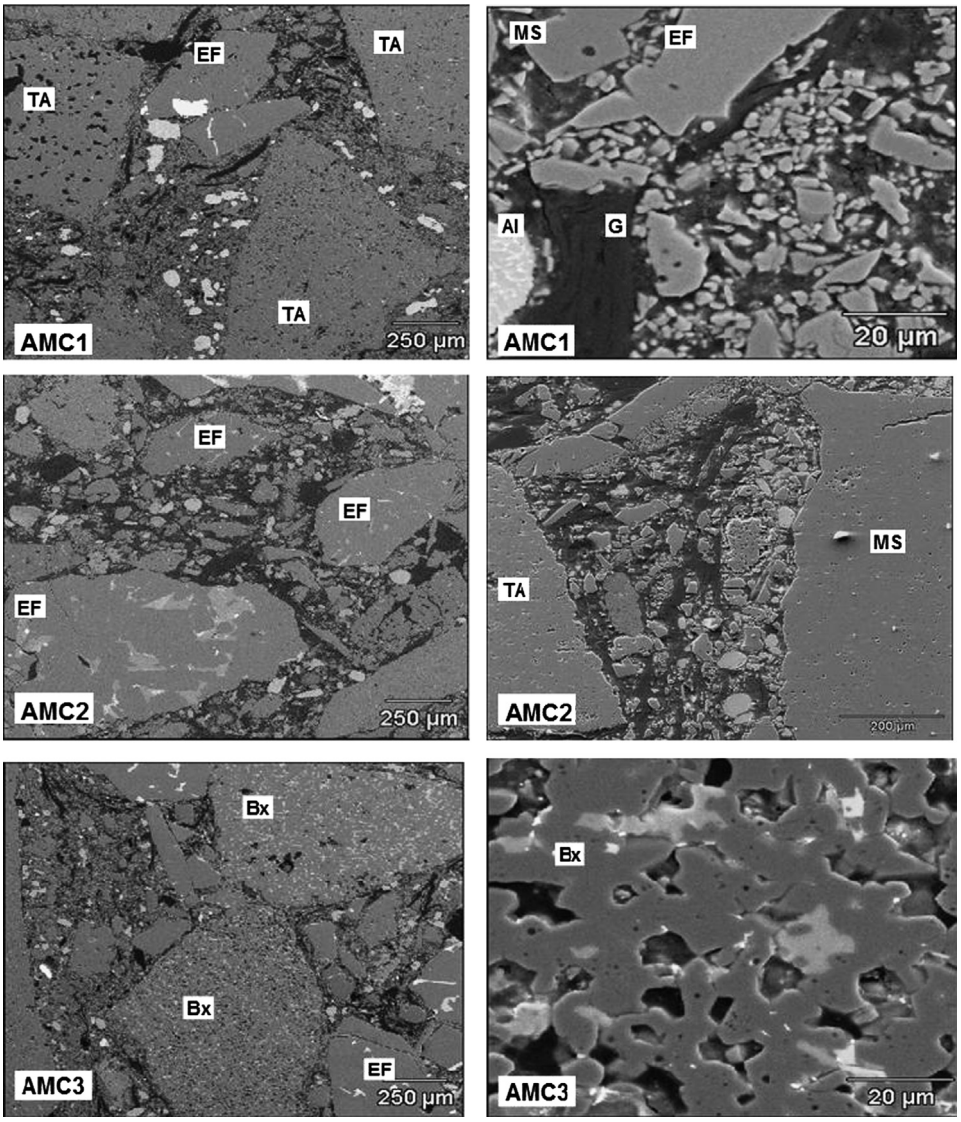

Fig. 2. SEM images of AMC refractories (TA: tabular alumina, EF: brown electrofused alumina, Bx: bauxite, MS: sintered magnesia, G: graphite, and Al: aluminum).

flow, Pt cells, alumina as reference material and a heating rate of 10 °C/min. The static thermal treatments were carried out between 400 and 1400 °C, in air, for 4 h using a heating rate of 10 °C/min. AMC brick fragments ~8 cm^3 in volume and an electrical furnace (Carbolite) with SiC heating elements were used. After the treatments, the fragments were ground and milled, and the mineralogical composition of the powders was determined by XRD using a Panalytical X´PERT PRO diffractometer, Cu Kα radiation, 40 kV, 40 mA, a monocromator, at a rate of 10°/min. Some of the thermally treated specimens were impregnated in polyester resin in vacuum. Their surfaces were polished (SiC paper up to 4000 grit and 1 μm diamond paste) and analyzed by SEM/EDS with a Philips XL30 microscope. To back up the analysis of DTA and TGA thermograms, free energy (ΔG) computations for possible reactions between Al, C, O_2, MgO and Al_2O_3 were performed using HSC [15]. This is a computing package that offers an exhaustive thermochemical database and includes enthalpy, entropy and heat capacity data for chemical compounds.

The dilatometric analysis was done using prismatic specimens ($30 \times 30 \times 50$ mm^3) up to 1400 °C, with heating and cooling rates of 2 °C/min, in argon gas flow. For determining the permanent linear change (PLC) of the AMC materials, specimens of $30 \times 30 \times 50$ mm^3 were successively subjected to five thermal cycles in air at 1400 °C in duplicate. The treatment was done in an electrical furnace (SiC heating rates) with a heating rate of 10 °C/min up to the selected temperature. The specimens remained at this temperature for 2 h with free cooling afterwards. After each cycle, the length along the prism axis was determined. The permanent linear change was considered as the variation of the length with respect to the initial value (*i.e.*, at the beginning of cycle 1). The apparent porosity of the treated specimens after cycles 1, 3 and 5 was also determined by applying the same methodology used for the original materials. In addition, the quantification of phases

was carried out by XRD on the powdered samples prepared by grinding and milling the specimens after cycle 1. A Panalytical X´PERT PRO diffractometer was used, with Cu Kα radiation, 40 kV, 40 mA, monocromator, and a rate of 10°/min. The Rielveld method (FULLPROF program) was used for the mineralogical quantification.

An Instron 8501servohydraulic mechanical testing machine was used to obtain stress (σ)–strain (ε) curves in compression. The tests were carried out in triplicate at room temperature, with a constant displacement rate of 0.1 mm/min. Cylindrical specimens 27 mm in diameter and 40 mm in height were tested. The dimensional variation along the cylinder axis was measured with an Instron capacitive extensometer ($\pm$0.6 μm). The following parameters were obtained from the stress–strain curves: (a) mechanical strength (σ_f), as the maximum value of the stress, and its corresponding deformation (ε_f), (b) Young's modulus, as the slope of the linear portion of the curves, and (c) yield stress (σ_y), defined as the stress where the curve deviates from the linear behavior. The ratio σ_y/σ_f, represented as a percentage, was considered as indicative of the deviation of the stress–strain curves from the linear behavior.

3. Results and discussion

3.1. Microstructural analysis

SEM images of the three AMC refractories are shown in Fig. 2, in which the presence of alumina aggregates of different types can be observed. Tabular alumina (TA) and brown electrofused alumina (EF) appear in each refractory, with bauxite (Bx) appearing only in AMC3. The proportion of tabular alumina aggregates was higher than that of EF aggregates in AMC1. Moreover, the amount of AT particles in AMC1 was greater than that contained in the other two refractories.

Taking into account the detection limit of the EDS technique ($\pm$0.5 wt%), the high purity of the tabular alumina used as a raw material (>99 wt%) was confirmed in each refractory. In the brown electrofused alumina aggregates, the corundum grains contain titanium in solid solution, with percentages of 1–2 wt% in the three AMC refractories. In the regions between the α-Al_2O_3 grains, the presence of crystalline and amorphous phases with SiO_2, MgO Al_2O_3, and TiO_{2-x} were detected. In the bauxite particles in AMC3, the SEM/EDS showed impurities of Ca and K in very low proportions (<0.5 wt%) and Si, Fe and Ti at a higher percentage (>1 wt%). Minor amounts of typical impurities such as mullite ($3Al_2O_3 \cdot 2SiO_2 = Al_6Si_2O_{13}$), tiellite ($Al_2O_3 \cdot TiO_2 = Al_2TiO_5$) and rutile ($TiO_2$) were observed together the main phase of corundum. The content of titania, ≈9 wt%, is somewhat greater than that recommended for the refractory use of bauxite (<4 wt% [16]), whereas the proportions of SiO_2 and Fe_2O_3, ≈2.5 and 1 wt%, respectively, are in agreement with the limits suggested in the literature (<2.5 wt% for both them [16]). SiO_2/TiO_2 in bauxite particles was ~0.3.

Coarse sintered magnesia particles with sizes up ~1 mm were only detected in the AMC2 refractory, which contains the highest MgO content according to both the technical data

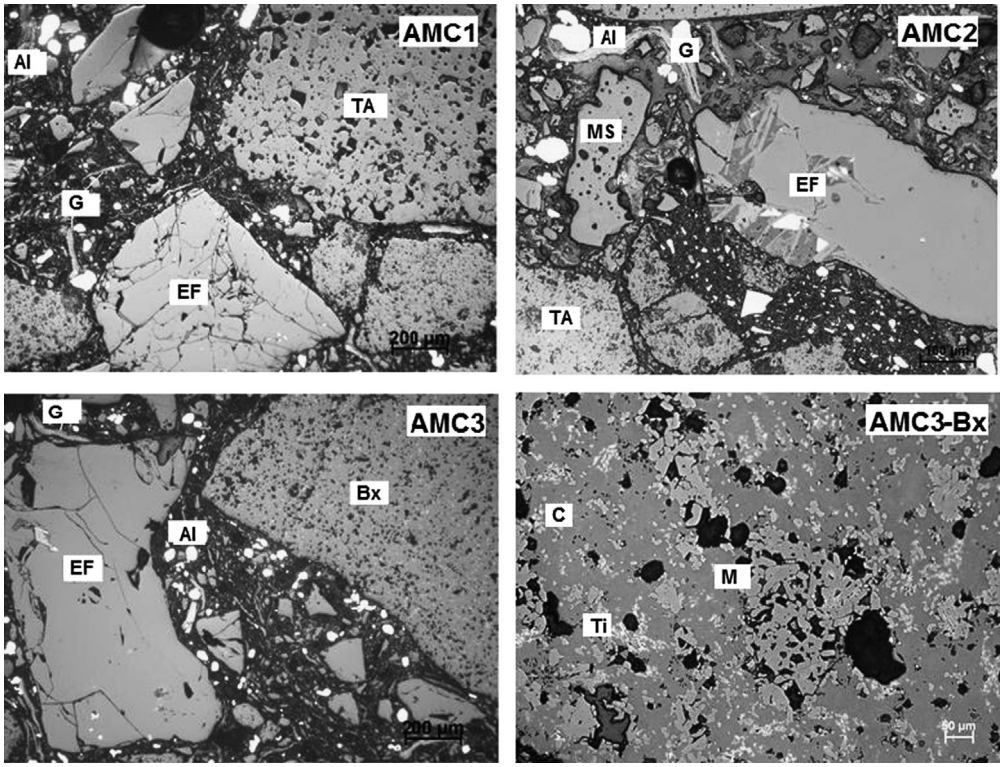

Fig. 3. Images of AMC refractories obtained by optical microscopy (TA: tabular alumina, EF: brown electrofused alumina, Bx: bauxite, G: graphite, Al: aluminum, C: corundum, M: mullite, and Ti: titanium-containing phase).

sheets and chemical analysis. In these particles, Al, Si, Ti and Na impurities were identified.

The microscopic analysis of the bonding phase revealed the presence of graphite flakes, metallic aluminum particles as well as fine particles of alumina and magnesia in each AMC refractory. The magnesia particles present in the fine fraction of AMC1, AMC2 and AMC3 have a purity < 96 wt%, with *Ca*, Fe and Si as the main secondary components, which corresponds with the typical impurities for this type of raw material. The graphite flakes of AMC1 and AMC2 showed a purity higher than 94 wt%, whereas those of AMC3 were purer (97 wt%). Between the minor components, Al and Si, which constitute the ashes that usually accompany graphite were detected in higher amounts, along with lower percentages of Mg and S. The aluminum particles exhibited a purity < 90 wt % in AMC1 and AMC3, with solutes such as Fe, Cu, Zn and Mn present. The aluminum was purer in AMC2 (> 90 wt%), although it contained impurities similar to those present in AMC1 and AMC3.

From the analysis by reflected light optical microscopy, the characteristics derived by SEM/EDS related to the raw materials used to formulate the bricks and their final microstructure were confirmed and complemented. Fig. 3 shows typical optical micrographs of the three AMC refractories.

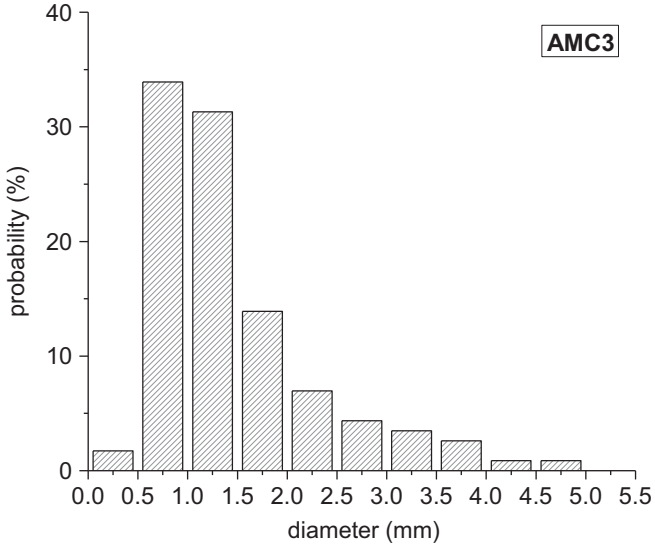

Fig. 4. Particle size distribution curve of oxide particles (> 0.1 mm) for AMC3.

Table 1
Statistical parameters of particle size distribution of alumina and magnesia (> 100 μm) and aluminum for AMC refractories.

	AMC1		AMC2		AMC3	
	Oxides[a]	*Al*	*Oxides*[a]	*Al*	*Oxides*[a]	*Al*
D_{max} (μm)	5170	105	3740	61	4860	120
D_{min} (μm)	260	3	214	4	400	18
D_{50} (μm)	650	27	480	11	980	34

[a] 'Oxides' includes alumina and magnesia.

Table 2
Proportion of oxide particles (> 0.1 mm) in number, in different granulometric ranges, for AMC refractories.

	0.2–1.00 mm	1.00–2.50 mm	2.50–5.50 mm
AMC1 (%)	70	27	3
AMC2 (%)	81	18	1
AMC3 (%)	52	38	10

Table 3
Proportion of aluminum particles in number, in different granulometric ranges, for AMC refractories.

	0–10 μm	10–50 μm	50–120 μm
AMC1 (%)	15	80	5
AMC2 (%)	43	55	2
AMC3 (%)	0	50	50

As an example, the particle size (> 0.1 mm) distribution curve for AMC3 is shown in Fig. 4. The estimated statistical parameters (D_{max}, D_{min} and D_{50}) that describe the granulometry of the coarser particles of alumina and magnesia in AMC refractories are given in Table 1. According to the obtained results, AMC2 has the smallest particles while AMC1 and AMC3 have similar granulometries. Nevertheless, D_{min} and D_{50} for AMC3 shifted to larger sizes.

Table 2 shows the proportion of oxide particles in three size ranges: 0.2–1.00 mm, 1.00–2.50 mm and 2.50–5.50 mm. The first range corresponds to the medium-sized fraction of particles while the last two ranges include the coarse fraction of particles. AMC1 and AMC2 have a high percentage of small aggregates (0.2–1.00 mm), very low medium-sized particle content (1.00–2.50 mm) and a scarce amount of large aggregates (2.50–5.50 mm). Using the aggregate characteristics observed by both the naked eye and microscopic analysis, it was possible to identify the small particles of AMC1 as white tabular alumina; these particles appear in higher proportion to the EF particles. The largest particles correspond to electrofused brown alumina, which possess a characteristic dark color detected by the naked eye. The greater amount of small particles in AMC2 could be related to its higher content of medium-sized magnesia particles (taking into account that the fine fraction of particles is not quantified by this method) and a lower proportion of alumina (tabular as well as brown/electrofused) with respect to AMC1 and AMC3. In the latter refractory, the difference between the number of particles from each of the three size ranges was less marked in comparison to the other two materials. In contrast with AMC1 and AMC2, the percentage of medium-sized particles (0.2–1.00 mm and 1.00–2.50 mm) in AMC3 is almost equivalent to that of the coarse particles (2.50–5.50 mm). This granulometric distribution leads to the higher value of D_{50} estimated for AMC3 (Table 1). Taking into account the observations made with the

Table 4
Length (L), thickness (A) and aspect ratio (L/A) of graphite particles contained in AMC refractories.

	AMC1	AMC2	AMC3
L_{max} (μm)	721	527	719
L_{min} (μm)	151	81	68
L_{50} (μm)	301	211	193
A_{max} (μm)	125	28	64
A_{min} (μm)	12	8	10
A_{50} (μm)	18	11	16
L/A_{max}	34	34	28
L/A_{min}	6	6	6
L/A_{50}	11	11	9

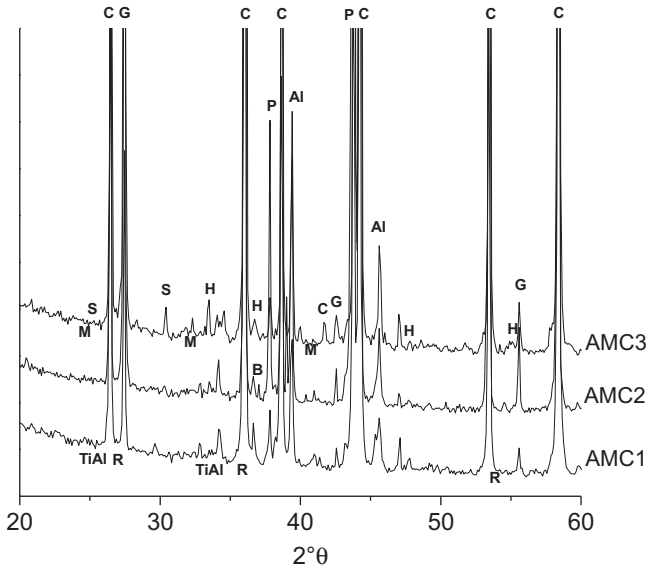

Fig. 5. X-ray diffractograms of AMC refractories (C: corundum, P: periclase, G: graphite, A: aluminum, H: hematite, M: mullite, R: rutile, S: pseudobrookite, and TiAl: aluminum titanate).

naked eye and microscopic analysis, it can be asserted that a large part of the coarser aggregates in AMC3 corresponds to brown electrofused alumina and bauxite particles.

The granulometric parameters for aluminum particles in the studied AMC refractories are indicated in Table 1. AMC3 contains the largest metallic particles, followed by AMC1. In AMC1, the finest particles have sizes similar to those found in AMC2. Table 3 summarizes the probability values for three ranges of aluminum particle sizes: 0–10 μm, 10–50 μm and 50–120 μm. Particles with sizes between 10 and 50 μm appear in abundance in the three AMC materials. Only AMC1 and AMC2 have very fine particles (<10 μm), with a higher proportion in the latter refractory. The amount of Al particles with diameters larger than 50 μm is significantly higher in AMC3 than in the other two materials, which explains the shifting of D_{50} to higher values.

Table 4 summarizes the values for the length (L), thickness (A) and the aspect ratio (L/A) of the graphite flakes. AMC1 and AMC3 contain the largest particles, with the former containing the thickest flakes. In general, the sizes of graphite particles are smaller in AMC2. In spite of these differences, the aspect ratios turned out to be similar in the three AMC materials.

3.2. Compositional analysis

The diffractograms of the three AMC refractories are plotted in Fig. 5, and the identified phases are indicated in Table 5 along with the ICDD files used [17]. The phases in parenthesis in Table 5 are those whose diffraction peaks weakly defined. The nature and estimated amount of the identified phases (Table 5) were consistent with the main constituents of the refractories according to the microstructural analysis. The major phase in each refractory is corundum (α-Al_2O_3), followed by periclase (MgO) and graphite. The presence of metallic aluminum as a minor phase was confirmed in each of AMC refractory. In contrast with the other two materials, the peaks corresponding to periclase in AMC2 exhibited intensities comparable to those of corundum due to the higher content of this component with respect to AMC1 and AMC3. For this same reason, peaks corresponding to brucite ($Mg(OH)_2$), formed by the superficial hydration of magnesia particles, were only detected for AMC2.

The phases whose peaks had low intensities (traces) correspond to impurities that usually accompany the main components. Traces of hematite (Fe_2O_3), which is a common impurity of magnesia, were detected in all the materials. Very low intensity peaks attributed to mullite, aluminum titanate, pseudobrookite, and rutile were detected for AMC3, in agreement with the results of the microscopic analysis. These second phases are associated with the corundum in bauxite and, with the exception of mullite, the brown electrofused alumina particles. In AMC1 and AMC2, peaks with very low intensity were attributed to TiO_{2-x} and aluminum titanate, and even though its peaks are less defined (the reason it appears in parentheses in Table 5), the possible presence of rutile cannot be ruled out for these two refractories.

Data pertaining to the chemical composition of the AMC refractories are given in Table 6. Aluminum content is very similar for all the materials (<2 wt%), as is the percentage of resin, which is somewhat higher than that reported in the literature for this type of refractory. However, AMC1 contains less graphite than the other two refractories. The total percentage of carbon is 7.1 wt% for AMC1, 9.1 wt% for AMC2 and 8.0 wt% for AMC3.

The amount of magnesia in AMC2 was almost five times higher than found in the remaining materials; the higher content of Fe_2O_3, SiO_2, CaO and other minor impurities in AMC2 compared to AMC1 is attributed to this fact. No B_2O_3, which is a typical impurity in magnesia grains coming from seawater, was detected by XRF. The higher percentage of graphite in AMC2 could also contribute to its level of SiO_2.

The content of free Al_2O_3 in AMC3 was lower than in AMC1 due to the presence of mullite in the aggregates of bauxite, which is also consistent with the greater proportion of SiO_2 in AMC3. The amount of Fe_2O_3 and TiO_2 increases in

Table 5
Mineralogical analysis (DRX) of AMC refractories.

Phase	*No. ICDD file*	AMC1	AMC2	AMC3
Corundum (α-Al_2O_3)	46-1212	Major	Major	Major
Periclase (MgO)	74-1225	Abundant	Abundant	Abundant
Graphite (C)	41-1487(2H)	Abundant	Abundant	Abundant
Aluminum (Al)	85-1327	Minor	Minor	Minor
Hematite (Fe_2O_3)	33-0664	Traces	Traces	Traces
Brucite ($Mg(OH)_2$)	44-1482	–	Traces	–
Mullite ($Al_6Si_2O_{13}$)	84-1205	–	–	Traces
Aluminum titanate (Al_2TiO_5)	41-0258	Traces	Traces	Traces
Rutile (TiO_2)	21-1276	Traces	Traces	Traces
Pseudobrookite (Fe_2TiO_5)	41-1432	–	–	Traces

Table 6
Chemical analysis of AMC refractories.

Component	*wt%*		
	AMC1	**AMC2**	**AMC3**
Al_2O_3	82.7 ± 0.3	57.6 ± 0.3	76.6 ± 0.3
Al^0	1.39 ± 0.02	1.37 ± 0.02	1.60 ± 0.02
Fe_2O_3	1.59 ± 0.02	1.99 ± 0.02	2.07 ± 0.02
MgO	5.40 ± 0.03	26.9 ± 0.1	6.80 ± 0.03
SiO_2	0.68 ± 0.01	1.16 ± 0.01	2.42 ± 0.01
K_2O	–	–	0.072 ± 0.005
P_2O_5	0.016 ± 0.002	0.040 ± 0.004	0.075 ± 0.004
CaO	0.14 ± 0.01	0.52 ± 0.01	0.30 ± 0.01
Cr_2O_3	0.090 ± 0.02	0.10 ± 0.02	0.15 ± 0.02
TiO_2	0.50 ± 0.01	0.80 ± 0.01	1.50 ± 0.02
MnO	0.024 ± 0.002	0.038 ± 0.002	0.025 ± 0.002
ZrO_2	0.031 ± 0.003	0.070 ± 0.003	0.20 ± 0.01
SrO	0.029 ± 0.003	0.041 ± 0.003	0.081 ± 0.003
ZnO	0.049 ± 0.004	0.052 ± 0.004	–
Graphite	1.7 ± 0.1	3.5 ± 0.1	3.0 ± 0.1
Resin	5.4 ± 0.1	5.6 ± 0.1	5.0 ± 0.1

Table 7
Mineralogical composition of AMC refractories according to rational analysis.

Component	*wt%*		
	AMC1	**AMC2**	**AMC3**
Al_2O_3	82.7	57.6	70.5
Al^0	1.4	1.4	1.6
MgO	5.4	26.9	6.8
Fe_2O_3	1.6	2.0	2.0
$Al_6Si_2O_{13}$	–	–	8.6
C (graphite)	1.7	3.5	3.0
Resin	5.4	5.6	5.0
Other impurities	1.6	2.8	2.7

the order: AMC1 < AMC2 < AMC3. The difference between AMC1 and AMC2 is consistent with a higher proportion of EF in AMC2 and a greater content of tabular alumina in AMC1 (derived from the microstructural analysis), whereas the more elevated percentage of these oxides in AMC3 is attributed mainly to the presence of bauxite. The total amount of impurities follows the order: AMC1 (1.6 wt%) < AMC2 (2.8 wt%) < AMC3 (4.9 wt%). This fact is consistent with the greater percentage of high purity tabular alumina in AMC1, sintered MgO, graphite and EF in AMC2, and bauxite in AMC3.

Taking into account the results obtained by XRD, SEM/EDS and the chemical composition data for AMC refractories, a rational analysis was carried out to quantify the phases, the considerations of which were explained in a paper published previously by the authors [9]. The proportions obtained from rational analysis for the main phases present in AMC refractories are given in Table 7.

3.3. Textural analysis

The density and porosity values of the studied refractories are given in Table 8. The picnometric densities are similar for the three materials, with the order AMC1 > AMC3 > AMC2. The small differences between ρ_{pic} values of the refractories (< 2%) are due to differences in the proportions and densities of the solids composing them. Taking into account the results of the chemical and microstructural analyses, AMC1 is the material with the highest amount of tabular alumina, which is the densest component of AMC refractories with a density ~3.9 g/cm^3. Only AMC3 contained calcinated bauxite, which has a lower density (3.1–3.5 g/cm^3) than tabular alumina. AMC2 possesses the lowest amount of alumina in the form of tabular and brown electrofused particles (density of EF: 3.92–3.94 g/cm^3), and it has the highest amount of those components with the lowest densities (sintered magnesia: ~3.4 g/cm^3, graphite: ~2.2 g/cm^3 and resin: ~1.2 g/cm^3).

Although the overall density of AMC1 is equivalent to that of AMC3, the apparent porosity of the latter is lower, which corresponds with its small value of ρ_{pic} and is mainly due to the presence of bauxite. AMC2 had the lowest value of ρ_g due to its greater volume of open pores (π_a) and lower picnometric density. The true porosity of the three materials follows the same order as their apparent porosity (AMC2 > AMC1 > AMC3) although the differences are less significant. AMC2 also resulted in having the greatest volume of closed pores; its higher graphite content could be one of the factors contributing to this fact [18].

Table 8
Density and porosity values of AMC refractories.

	ρ_{pic} (g/cm^3)	ρ_g (g/cm^3)	π_a (%)	π_c (%)	π_v (%)
AMC1	3.45 ± 0.20	3.14 ± 0.02	6.7 ± 0.1	2 ± 2	9 ± 2
AMC2	3.37 ± 0.08	2.98 ± 0.01	7.8 ± 0.5	4 ± 2	12 ± 2
AMC3	3.39 ± 0.02	3.14 ± 0.1	4.0 ± 0.1	3 ± 2	7 ± 2

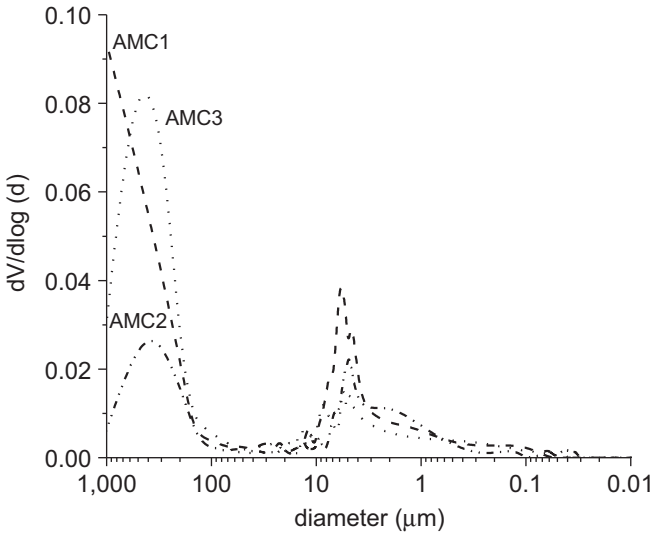

Fig. 6. Pore size distributions of AMC refractories.

The distribution of pore sizes was bimodal for each of the AMC refractories, as shown in Fig. 6. The pore sizes >100 μm correspond to packing defects and those <100 μm are small pores located between fine particles in the matrix and the intraparticle pores. The parameters for pore size distributions are given in Table 9 as maximum (D_P^{max}), minima (D_P^{min}) and the most probable value (D_P^{mp}), with the latter being defined as the diameter contributing most to the pore volume (highest probability of occurrence). The three AMC materials have approximately the same maximum diameter for pores larger than 100 μm, although the most probable diameter in this size range followed the order: AMC1 > AMC2 > AMC3. In the case of pores <100 μm, D_P^{mp} was the same for the three refractories, but the smallest pore size ($D_P^{mín}$) decreased in the order AMC1 > AMC2 > AMC3. Overall, it was concluded that AMC1 has the largest pores and AMC3 has the smallest pores. Moreover, AMC3 has the least volumetric fraction of open pores whereas AMC2, which has the greatest apparent porosity, contains pores intermediate in size between the other two refractories.

Permeability is a property linked to the interconnected porosity and is closely related to the open porosity and pore sizes. Pores are considered to be capillaries in the models used to determine the permeability of a solid body [19,20]. The permeability curves determined for each AMC refractory are plotted in Fig. 7. The values for AMC3 are remarkably lower than the other materials, which corresponds to its low apparent porosity and pore sizes. At the opposite end, the highest permeability was displayed by AMC2, which has the greater volumetric fraction of open pores. The tortuosity parameter determined by the applied technique was ~2 for the three AMC refractories.

3.4. Thermal evolution analysis

The thermograms obtained by DTA and TGA for each of AMC refractories are shown in Figs. 8 and 9, respectively. The mass changes displayed in TGA curves are given in Table 10. The DTA graphs show peaks between 350 and 650 °C that are attributed to the transformation of resin [21,22] and the oxidation of residual carbon (glassy-carbon), which would occur at approximately 630 °C for each material. The differences in the amount, position and intensity of the DTA peaks in this temperature range could indicate that each of the refractories contains a different type of resin. However, the presence of different inorganic components also affects the resin pyrolysis [21] and could be the reason for the differences mentioned above. This second alternative may be supported by the fact that all the bricks were of the same material type and made by the same manufacturer. Nevertheless, there is not enough experimental evidence available to make any decisions regarding the similarity or disparity of the resins' characteristics for each refractory.

Both processes concerning the resin carbonization and the oxidation of the residual carbon are accompanied by weight loss due to the evolution of gases. The differences in the loss of mass between the AMC refractories below 700 °C (Table 10) are linked to differences in the resin contents. The percentage of resin estimated from the Δm values in Table 10 was determined to be 4–5 wt% for AMC1, ~6 wt% for AMC2 and ~4 wt% for AMC3, which is similar to the contents determined by gravimetry for the thermal treated samples (Table 6). The intensity of the peaks corresponding to the oxidation of the glassy-carbon corresponds with the small differences in the proportion of resin, which is well defined in AMC2 and rather less defined in AMC3. The same happens with the weight loss displayed between 600 and 670 °C, which could correspond to the elimination of the residual carbon as CO_2 (g).

A little endothermic peak was observed in the range 650–665 °C produced by the melting of aluminum. This peak was not seen in the thermograms of AMC2 even at lower heating rates; this fact is attributed to the fine granulometry of this refractory's aluminum particles, which might accelerate the melting process and decrease the definition of the DTA peak. Accordingly, the peak was very clear for AMC3, which contains the coarsest aluminum particles, and was hardly

Table 9
Statistical parameters of pore size distributions for AMC refractories.

	Pore diameter			
	> 100 μm		**< 100 μm**	
	D_P^{max}[a] **(mm)**	D_P^{mp}[b] **(mm)**	$D_P^{mín}$[c] **(μm)**	D_P^{mp} **(μm)**
AMC1	≈ 1	0.90	0.060	6.00
AMC2	≈ 1	0.50	0.055	6.00
AMC3	≈ 1	0.35	0.003	6.00

[a]Maximum pore diameter.
[b]Diameter with the maximum probability of occurrence.
[c]Minimum pore diameter.

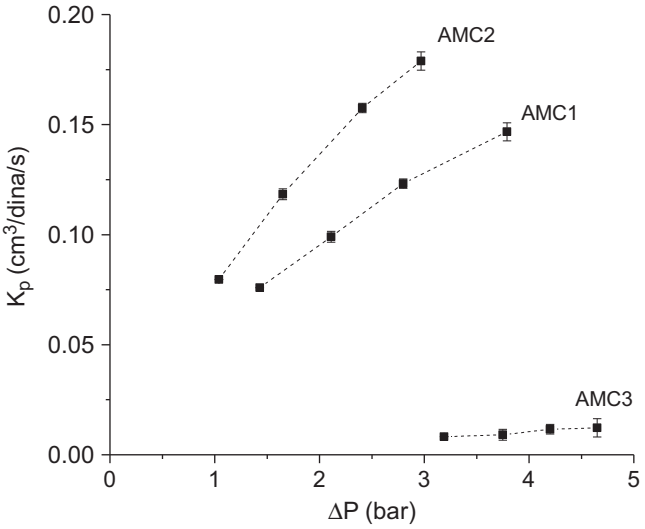

Fig. 7. Permeability of AMC refractories.

observed for AMC1. With respect to the melting point of pure metallic aluminum (660 °C), the temperature of the endothermic peaks was lower due to the presence of other elements dissolved in the Al-particles, as was confirmed by the SEM/EDS, and which reduces the melting temperature.

At approximately 900–990 °C, the oxidation of graphite occurred accompanied by weight loss somewhat higher than 1 wt% for AMC1 and approximately 3 wt% for AMC2 and AMC3. These values are similar to those determined in a more accurate manner by gravimetry (Table 6). The maximum temperature of the DTA peak was slightly higher for AMC3 than for AMC1 and AMC2; this fact indicates a higher resistance of the graphite to be oxidized, which was attributed to the higher purity of the flakes in AMC3.

DTA peaks with low definition and intensities were observed at temperatures > 1000 °C. These were attributed to the aluminum's reaction with the diverse components of the refractories [23–26]. Some of the chemical processes that occur between 1000 and 1400 °C and after the melting and/or vaporization of aluminum are given below:

$$4Al_{(l)} + 3C_{(s)} \rightarrow Al_4C_{3(s)} \quad \Delta G_R^{1000\ ^\circ C} = -32.1\ \text{kcal}, \quad \Delta m = 0/\Delta V = +9\% \tag{1}$$

$$Al_4C_{3(s)} + 3O_{2(g)} \rightarrow 2Al_2O_{3(s)} + 3C_{(s)} \quad \Delta G_R^{1000\ ^\circ C} = -575.2\ \text{kcal}, \quad \Delta m = +67\%/\Delta V = +50\% \tag{2}$$

$$MgO_{(s)} + 2Al_{(l)} \rightarrow MgAl_2O_{4(s)} + 3Mg_{(g)} \quad \Delta G_R^{1000\ ^\circ C} = +24.1\ \text{kcal}, \quad \Delta m = -34\%/\Delta V = -40\% \tag{3}$$

$$MgO_{(s)} + Al_2O_{3(s)} \rightarrow MgAl_2O_{4(s)} \quad \Delta G_R{}^{1000\ ^\circ C} = -3.4\ \text{kcal}, \quad \Delta m = 0\%/\Delta V = +8\% \tag{4}$$

When these reactions occur, they are usually accompanied by changes in mass (Δm), which are indicated for each of them. Taking into account just the reactions involving $\Delta m > 0$ and the amount of Al present in the analyzed refractories, increases of between 0.9 and 2.0 wt% were calculated, which is consistent with those values obtained from TGA in this range of temperatures.

The results of the thermal evolution study on the refractory brick fragments, which were previously reported in another paper [11], confirmed the similarity in the behavior of the three AMC materials. It was established that graphite was completely lost at 1000 °C, and the amount of aluminum decreased when the abovementioned reactions began. Furthermore, the presence of Al_4C_3 was confirmed between 1000 and 1200 °C, and the formation of $MgAl_2O_4$ spinel was detected from 1100 °C onward, while at the same time the amount of magnesia decreased. The spinel content increased as the temperature increased. At 1400 °C, no magnesia was detected in AMC1, but this oxide was still present in AMC2 and AMC3.

It was inferred by SEM/EDS analysis of the thermally treated fragments that the $MgAl_2O_4$ phase identified by XRD from 1100 °C was formed by more than one reaction mechanism in each of the AMC refractories, *i.e.*, the combination of MgO with: (a) Al, (b) the products resulting from the reaction of the aluminum, and/or (c) Al_2O_3 particles, including aggregates. SEM images of AMC1 treated at 1370 °C are shown in Fig. 10 at different magnifications, and the formation of spinel (MA) with different aspects and location can be observed. Spinel was detected around the void left by the aluminum

when it melted and reacted with other refractory components (Fig. 10a), including magnesia, which is a typical texture in carbon-containing refractories with Al. This mechanism has been described by Zhang et al. [27]. Furthermore, spinel formed within the matrix, with a foamed texture characteristic of the combination of MgO and Al_2O_3 in solid state (Fig. 10b and c) accompanied by pore generation [25,28]. The dispersal of the MA phase in the matrix was considered to be caused by the combination of the more reactive fine particles of magnesia and alumina. However, spinel was also identified in regions alongside alumina aggregates (Fig. 10b and c), which indicates that these coarse particles also served as sources of alumina.

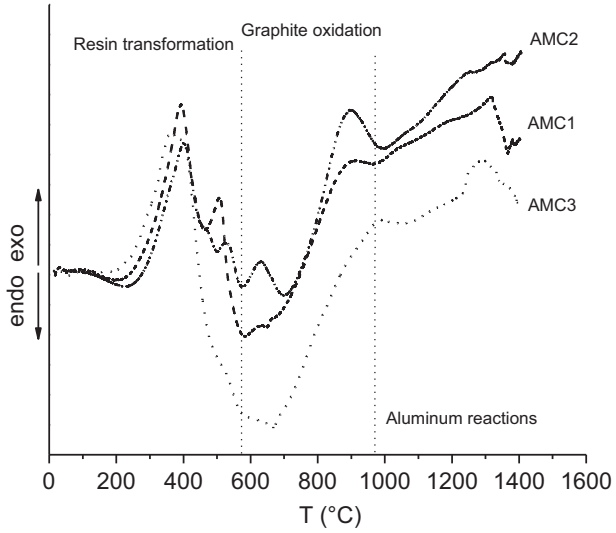

Fig. 8. DTA thermograms of AMC refractories.

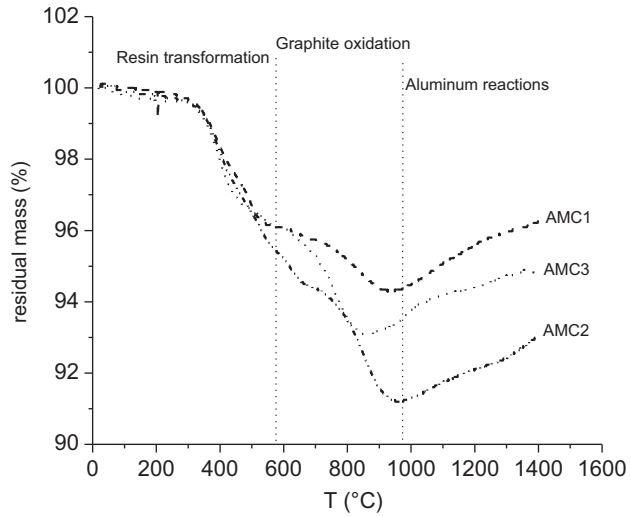

Fig. 9. TGA thermograms of AMC refractories.

3.5. Dimensional change analysis

In Fig. 11, the variation of dL/L_0 (change of the specimen's length as a percentage) as temperature increased (in the heating step) for AMC1, AMC2 and AMC3 refractories is shown. The dilatometric curves show an overall behavior that is similar for all three AMC refractories, which corresponds to the similarity shown in the transformations undergone by the materials as temperature increased.

At temperatures $<700\ ^\circ C$, shrinkage was observed in the three AMC materials, which is attributed to the transformation of the organic binder and accompanied by a volumetric contraction [22]. The change in dL/L_0 up to 600 °C was similar for AMC1 and AMC3, and there were two temperature ranges within which length varied negatively: up to 400 °C and from 400 to 600 °C, with the largest contraction occurring at approximately 600 °C. However, the minimum dL/L_0 was quite higher for AMC3 (up to $\sim -0.2\%$) compared to AMC1 (up to $\sim -0.04\%$). In addition, the dilatometric curve for AMC2 only shows the first shrinkage stage, with an intermediate value of dL/L_0 (-0.13%). The differences in dilatometric behavior at temperatures $<700\ ^\circ C$ cannot be justified by the differences in resin content because they are very similar for the three materials. If this were not the case, this could be explained by differences in the ability of the refractory microstructure to absorb the volumetric shrinkage caused by the resin pyrolisis, which in turn would be linked to different degrees of cohesion between the organic binder and the rest of the matrix components. Taking this into account, AMC3 would have, from an overall point of view, the highest affinity between the resin and the rest of inorganic phases, followed by AMC1 and then AMC2.

Table 10
Assignment of the loss/gain of mass (Δm) identified by TGA.

AMC1		AMC2		AMC3		*Assignment*
Δm (wt%)	**T^a (°C)**	**Δm (wt%)**	**T^a (°C)**	**Δm (wt%)**	**T^a (°C)**	
−2.3	373	−2.4	380	−3.0	392	Resin transformation
−1.8	486	−2.2	498	−0.3	534	
−0.5	667	−1.1	622	−0.3	600	Glassy−C oxidation
−1.3	826	−3.2	833	−3.0	740	Graphite oxidation
1.6	1092	1.0	1082	0.86	962	Formation of Al_2O_3 and/or $MgAl_2O_4$
0.4	1344	1.0	1326	0.42	1186	
				0.4	1274	

[a]Temperature corresponding to half of the loss/gain of mass.

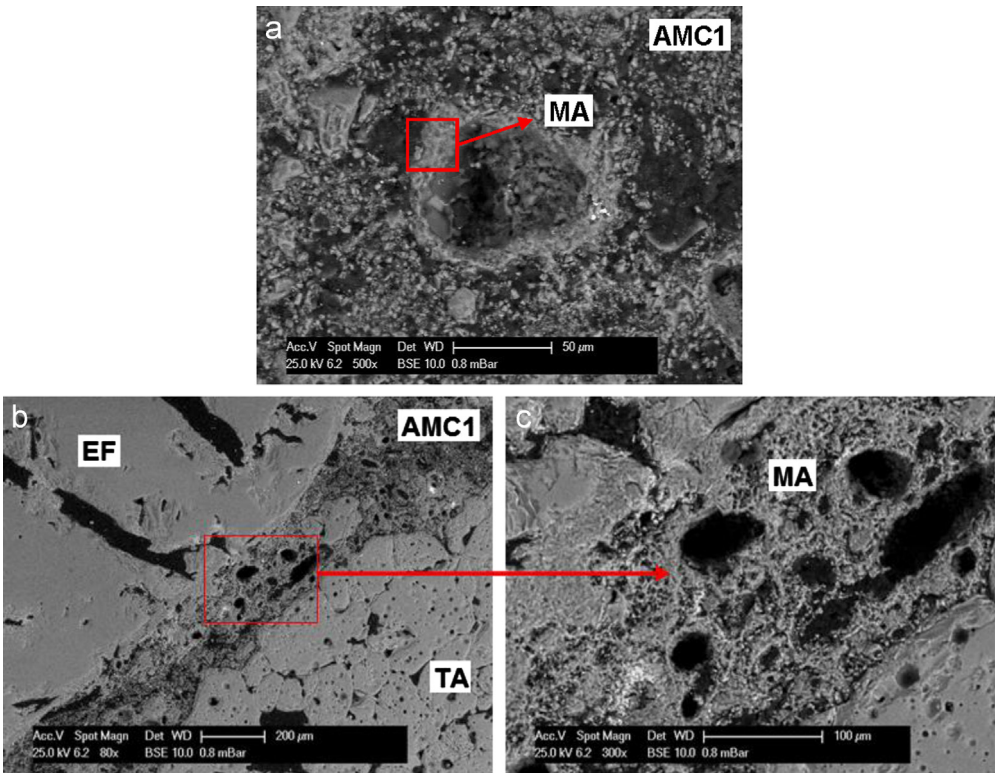

Fig. 10. SEM images of AMC1 treated at 1370 °C (TA: tabular alumina; EF: brown electrofused alumina; and MA: $MgO \cdot Al_2O_3$ spinel).

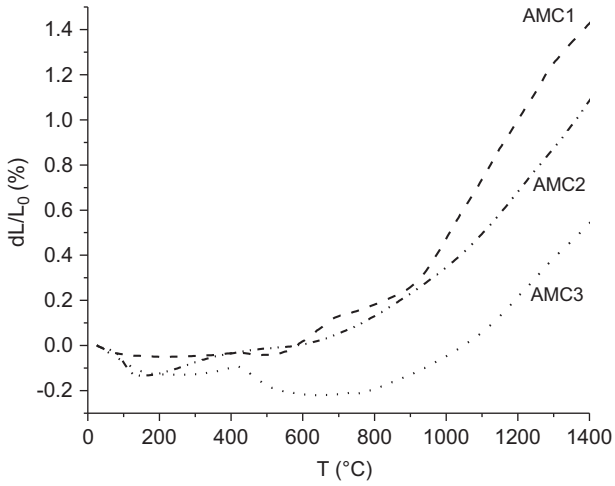

Fig. 11. Dilatometric curves of AMC refractories.

In the 700–1000 °C range, the dilatometric curves show a linear expansion, with a slope of 7.3×10^{-6} °C^{-1} for AMC1, 8.9×10^{-6} °C^{-1} for AMC2 and 8.1×10^{-6} °C^{-1} for AMC3. In this temperature region, the resin was completely carbonized, and the oxidation of graphite begins, thus each AMC refractory can be considered as formed mainly by the inorganic components. In fact, the linear expansion coefficient estimated by the mix rule and the mineralogical composition of each refractory (Table 7) was between 8 and 10×10^{-6} °C^{-1}.

At temperatures slightly higher than 1000 °C, a significant change in the slope of the dilatometric curves is seen, followed by a linear expansion stage up to 1300–1350 °C. The slope of these regions is significantly high: 27×10^{-6} °C^{-1} for AMC1, 19×10^{-6} °C^{-1} for AMC2 and 17×10^{-6} °C^{-1} for AMC3. According to the DTA thermograms (Fig. 8), several processes are initiated in this temperature range, usually accompanied by volumetric changes (ΔV), as was indicated in reactions [1–4]. The expansive reactions are those involving gaseous species such as O_2, CO_2 or CO, which can be present in the system as impurities from the Ar flow during the test and byproducts of resin carbonization, graphite oxidation (although these reactions are diminished due to the low oxygen content of the atmosphere) and/or Al_4C_3 decomposition. Furthermore, it must be taken into account that the formation of spinel in solid state, for instance, leads to additional volume expansion due to pore generation, which can also contribute to an increase in the value of dL/L_0.

The dilation that occurred at the end of the heating process (1400 °C) resulted in the following values: 1.4% for AMC1, 1.1% for AMC2 and 0.5% for AMC3. The total expansion of AMC3 is remarkably lower than that of the other refractories, which could indicate that, (a) AMC3 has a lower global thermal expansion coefficient, (b) expansive reactions have occurred to a lesser degree in AMC3 or (c) the microstructure of AMC3 has accommodated the volumetric variations in a more efficient way. This accommodation may take place by mechanisms such as the crystallization of new phases into pores, microcracking and/or the sliding of material by viscous flow due to low melting point phases. The latter seems more probable due to the higher level of impurities of AMC3.

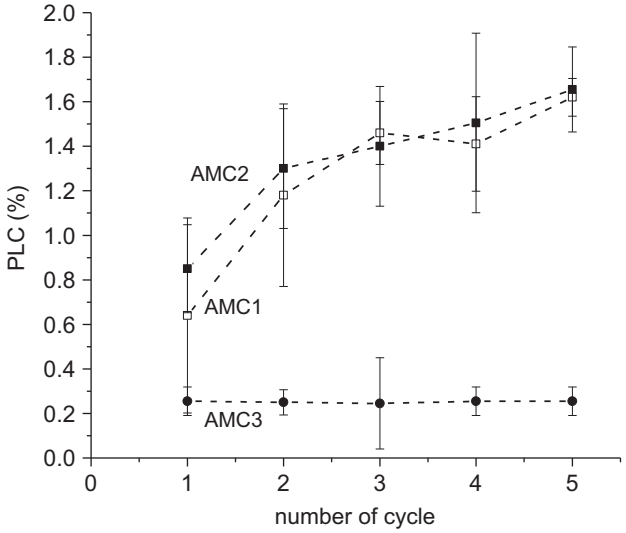

Fig. 12. Variation of the permanent linear change (PLC) of AMC refractories with the cycle number at 1400 °C.

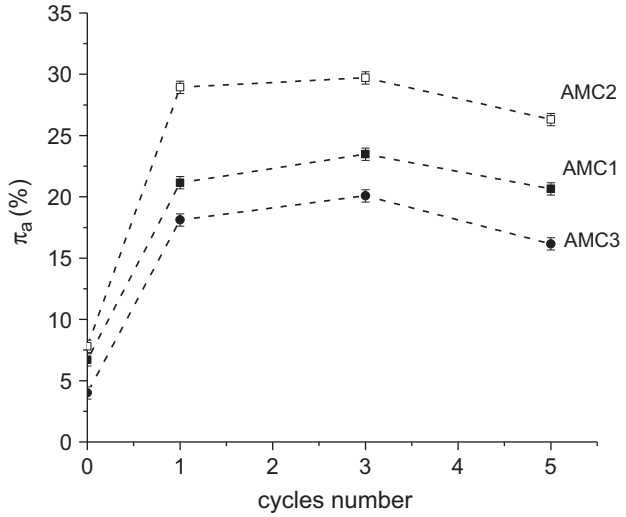

Fig. 13. Apparent porosity (π_a) of AMC refractories treated at 1400 °C (cycle 1).

In fact, the slope of the linear region at $T > 1000$ °C is always higher for AMC3 than for the other refractories.

The variation in the permanent linear change (PLC) of the studied AMC refractories as a function of the number of cycles at 1400 °C is plotted in Fig. 12. AMC1 and AMC2 show similar PLC values, which show a clear tendency to increase as the number of cycles increases. PLC values for AMC3, however, remained practically unchanged at 0.25% during the five cycles. The primary contributor to residual expansion at 1400 °C is spinel formation, which continues to increase as temperature and heating time increase. Miglani et al. [29] reported that the permanent linear change increased with temperature as the number of cycles and magnesia content increased. This explains the evolution of PLC for AMC1 and AMC2 although the similarity between the values of both materials is unexpected taking into account the differences in these refractories' composition and dilatometric behavior.

The small PLC value of AMC3 after each cycle at 1400 °C is consistent with the dilatometric analysis results, from which its lower dilation with respect to the two other materials was inferred. However, it would be expected that the change in PLC with the number of cycles would be similar to AMC1 due to the similarities in composition between AMC1 and AMC3, at least with regard to the content of MgO, which is a determining variable in the increased formation of spinel [28,29].

The variation in apparent porosity (π_a) of the specimens treated at 1400 °C as the number of cycles increases is plotted in Fig. 13 for each of AMC materials. The open porosity of each refractory treated at 1400 °C increases from cycle 1 to cycle 3, with the relative order the same for the three cycles (AMC3 < AMC1 < AMC2). The main change in π_a was seen after the cycle 1, with a higher additional volumetric fraction of pores for AMC2 ($\approx +21\%$) and similar values for the other two materials ($\approx +14\%$). This occurred during the first treatment due to the evolution of volatiles from the resin pyrolisis and graphite oxidation, which are sources of pores and fissures. Other processes leading to an increase in open pores could have also played a role, such as the oxidation of impurities and spinel formation. Finally, the apparent porosity decreased after cycle 5 at 1400 °C, which is attributed to the crystallization of new phases (mainly spinel) and/or the sintering of the fine particles. Even so, the residual expansion still increased with the successive cycles in AMC1 and AMC2 due to continued increase of the expansive reactions.

On the other hand, the amount of $MgAl_2O_4$ spinel in samples analyzed by quantitative XRD was 21 wt% for AMC1 and 14 wt% for AMC2 and AMC3. These data indicate that spinel forms more easily in AMC1 since the amount reached equals the quantity calculated if all of the available MgO reacts (21 wt%). This higher tendency of spinel formation in AMC1 was revealed by the disappearing of peaks of periclase in the AMC1 specimen treated at 1400 °C in air (Section 3.4) and the higher slope of the dilatometric curve at temperatures higher than 1000 °C (Fig. 11). This could be linked to a higher proportion of fine and/or smaller sizes of alumina (possibly tabular alumina) and magnesia particles. In spite of the fact that AMC3 has a similar nominal content of magnesia with respect to AMC1, a rather smaller amount of spinel formed in the former; this agrees with the results from the thermal evolution study, which showed that the magnesia remained in AMC3 after treatment at 1400 °C. In addition, a similar amount of spinel was formed in AMC3 and AMC2, which is inconsistent with what would be expected considering the greater proportion of MgO in the latter. However, it has been reported that MA spinel forms faster with smaller size of periclase particles [30]. Since AMC2 contains a wide range of magnesia particle size (within fine, medium-size and coarse fractions), it could be possible that the proportion of the fine fraction which is prone to react and form spinel result lower than that present in AMC1 and AMC3.

The factors considered as determinants in changing the PLC values after the cycles at 1400 °C are, the increase in open porosity, the occurrence of expansive reactions and the ability of the structures to absorb the volumetric variations. In the case of AMC1, the high degree of spinel formation and the increase of apparent porosity led to residual expansion after the first treatment at 1400 °C; in the successive cycles, this expansion was higher and mainly determined by the second factor. In comparison with AMC1, the spinelization occurred to a lesser degree in AMC2, but the volume fractions of open pores increased more, in part due to the larger size of the magnesia particles, which led to a similar residual expansion. As both processes advanced, PLC increased with the number of treatments. AMC3 showed an increase in apparent porosity similar to that of AMC1, but the increased spinel formation was equivalent to that of AMC2. The combination of both factors justifies the low residual expansion shown by AMC3, but it does not explain the constancy of PLC after the successive cycles. This behavior is considered a consequence of the ability of AMC3 to accommodate volumetric variations into its structure (as inferred from the volumetric analysis) by any of the mechanisms proposed above (crystallization of new phases into pores, microcracking and/or material sliding by viscous flow facilitated by this refractory's high level of impurities).

3.6. Analysis of mechanical properties at room temperature

Typical stress–strain curves of the three AMC refractories are shown in Fig. 14, and the mechanical parameters calculated from these curves are given in Table 11. The refractories show the typical quasi-brittle behavior of these materials: the stress–strain relationship is linear at the beginning, and then it becomes non-linear until specimen fracture. The values of σ_y/σ_f also manifest this behavior to a similar degree in the three AMC refractories. The non-linearity of stress–strain curves for this type of material is associated mainly with the sliding of the basal planes, the crumpling of the graphite flakes and microcracking [31,32]. Other less significant causes are the microplasticity of the organic binder and the stress relief introduced during the brick manufacturing process [32,33].

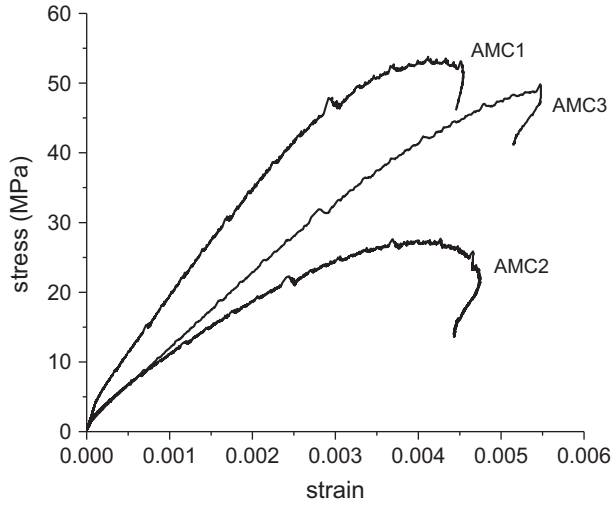

Fig. 14. Stress–strain curves of AMC refractories at room temperature.

Table 11
Mechanical parameters of AMC refractories.

	E (GPa)	σ_f (MPa)	ε_f	σ_y/σ_f (%)
AMC1	23 ± 10	52 ± 2	0.3 ± 0.1	68 ± 4
AMC2	11 ± 2	25 ± 2	0.3 ± 0.1	63 ± 15
AMC3	9 ± 2	46 ± 9	0.6 ± 0.1	65.4 ± 0.2

The stiffness of AMC1 was higher than that of AMC2 and AMC3, which have very similar Young's modulus values. These differences are related to AMC1's lower capacity to deform, which is due to its lower graphite content and higher proportion of tabular alumina (stiffer and more resistant than the other sources of alumina, brown electrofused alumina and bauxite).

In contrast, the fracture strength of AMC1 was highest, followed by AMC3 and AMC2, which has a significantly lower value. The main reason for this is that AMC2 has a large volume of pores and a greater proportion of the least-resistant components, sintered magnesia and brown electrofused alumina. AMC3, with bauxite as the alumina raw material, has an intermediate value of σ_f, but it has a higher fracture strain with respect to the other refractories, which have similar ε_f values. The latter values could be indicative of the higher affinity between the refractory components that was inferred from the dilatometric analysis of AMC3 and which reduces the ability of the structure to accommodate the strain imposed by the mechanical loading (opposite to what happens when the temperature was increased).

4. Conclusions

By applying a varied group of experimental techniques and conducting a detailed analysis of data, an exhaustive description of the different AMC commercial refractories studied here was achieved. The materials were characterized from several points of view, and the obtained data also served to explain certain aspects of their thermal evolution in relation to mineralogical and volumetric changes, as well as their mechanical behavior at room temperature. However, some features of the matrix, such as the granulometric distribution of fine particles of the oxides, which have a fundamental role in the mechanical and chemical behaviors of these materials, could not be evaluated using the methodologies available.

The main conclusions that can be drawn regarding the characteristics of the three AMC commercial bricks studied here are the follows:

– The major crystalline phase of these refractories is corundum (α-Al_2O_3) in the form of tabular alumina, with a higher proportion in AMC1. Brown electrofused alumina is found in all of the materials, but bauxite only appears in

AMC3. The second crystalline phase is periclase (MgO) in the form of sintered magnesia, with a proportion five times higher in AMC2 with respect to the other two materials. AMC1 and AMC3 only have magnesia in the fine fraction of particles whereas AMC2 also has medium-sized magnesia particles. The graphite flakes, with a similar aspect ratio for all three refractories, are smaller in AMC2, but their content is higher, whereas AMC3 possesses the purest graphite particles. Each refractory has a similar metallic aluminum content as an antioxidant additive.

- The total content of impurities, which is consistent with the minority phases that usually accompany the raw materials, follows the order: AMC1 < AMC2 < AMC3. The three materials are formulated with a similar phenolic resin content although the nature of this binder (novolaka or resol) could not be determined with the available techniques.
- The oxide particle sizes of medium-sized and coarse fractions and aluminum particles are generally larger in AMC3, with AMC2 exhibiting the smallest particles of these components. The smaller aggregates are tabular alumina and the larger particles correspond to brown electrofused alumina.
- The true porosity of the three materials follows the same order of the apparent porosities: AMC2 > AMC1 > AMC3. The AMC2 refractory also has the highest volume fraction of closed pores. AMC1 possesses the largest pores, and AMC3 the smallest pores; the permeability values of AMC3 are significantly lower than for the other two materials.
- The AMC refractories evolve in a similar way between 400 and 1400 °C in air, with the same transformations occurring: resin carbonization, residual carbon oxidation, graphite oxidation, the melting of aluminum, Al_4C_3 formation and $MgO \cdot Al_2O_3$ spinel formation. This last reaction occurs due to several mechanisms acting on the three materials, and it increases to a higher degree in AMC1, which is due likely to the finer granulometry of the alumina and magnesia particles in the matrix.
- The dilatometric curves for the refractories show that AMC3 has both reversible expansion and residual expansion that is less than the other two materials even when the value of PLC remains low and constant after successive treatments at 1400 °C. Furthermore, the results show that AMC3 possesses mechanisms that allow it to absorb the volumetric variations produced by the chemical changes at high temperature in a better manner than AMC1 and AMC2.
- The three refractories exhibit a quasi-brittle behavior when they are compressed, which is typical for this type of material. AMC1 and AMC3 are more resistant than AMC2 due mainly to the differences in mineralogical composition. Furthermore, AMC2 and AMC3 have a similar stiffness, which is lower than that of AMC1, which in turn corresponds to their respective amounts of graphite.

Aknowledgments

This work was supported by the Agencia Nacional de Promoción Científica y Tecnológica (ANPCyT) of Argentina under Project "Degradación termoquímica y termomecánica de refractarios óxido-C de uso siderúrgico", PICT2006 No. 1887) and the Spanish Government under Project no. MAT2010-17753. The authors would like to thank Dr. P.G. Galliano for the providing the material and participating in useful discussions and P. Ortega, M.J. Velasco and Dr. M.A. Rodriguez for implementing the chemical analysis and permeability methodologies.

References

[1] R.K. Koley, K.A.V. Rao, S. Askar, S.K. Srivastava, Development and application of Al_2O_3–MgO–C refractory for secondary refining ladle, in: Proceedings of the UNITECR'01, 2001.
[2] G. Büchel, X. Liu, A. Buhr, J. Dutton, Review of tabular alumina as high performance refractory material, Interceram—Refract. Man. 2007 (2007) 6–12.
[3] J. Pötschke, T. Deinet, G. Routschka, R. Simmat, Properties and corrosion of AMC-refractories. Part I: characterisation and oxidation, in: Proceedings of the UNITECR'03, 2003, pp. 580–583.
[4] Y. Sasajima, T. Yoshida, S. Hayama, Effect of composition and magnesia particle size in alumina–magnesia–carbon refractories, in: Proceedings of the UNITECR'89, 1989, pp. 586–603.
[5] A. Watanabe, H. Takahashi, S. Takanaga, N. Goto, O. Matsuura, S. Yoshida, Thermal and mechanical properties of Al_2O_3–MgO–C bricks, Taikabutsu Overseas 10 (1990) 137–147.
[6] A.D. Gupta, K. Vickram, Development of resin-bonded alumina–magnesia–carbon bricks for steel ladle applications, Interceram 48 (1999) 307–310.
[7] M. Kamiide, S. Yamamoto, K. Yamamoto, K. Nakahara, N. Kido, Damage of Al_2O_3–MgO–C brick for ladle furnace, J. Tech. Assoc. Refract. Jpn. 21 (2001) 252–257.
[8] A.H. De Aza, F.J. Valle, P. Ortega, P. Pena, S. De Aza, Analytical characterization of a magnesia–graphite refractory, J. Am. Ceram. Soc. 89 (2006) 1704–1708.
[9] P. Ortega, M.J. Velasco, V. Muñoz, P. Pena, A.G Tomba Martínez, Caracterización analítica de refractarios de Al_2O_3–MgO–C, Bol. Soc. Esp. Ceram. Vidr. 51 (2012) 305–312.
[10] DIN EN 993-1 (DIN 51056), Method of test for dense shaped refractory products. Determination of bulk density, apparent porosity and true porosity, 1995.
[11] V. Muñoz, A.G. Tomba Martínez, Thermal evolution of Al_2O_3–MgO–C refractories, Proc. Mater. Sci. 1 (2012) 410–417.
[12] V. Muñoz, G.A Rohr, A.L Cavalieri, A.G. Tomba Martinez, Experimental methodology for mechanical evaluation of oxide-carbon refractories by strain measurement, J. Test. Eval. 40 (2012) 1–9.
[13] ASTM C 1099-92, Standard test method for modulus of rupture of carbon-containing refractories materials at elevated temperaturas, 1992.
[14] ASTM C 133-94, Standard test methods for cold crushing strength and modulus of rupture of refractories, 1994.
[15] Outokumpu Research Oy, Pori, Finland Outokumpu HSC Chemistry for Windows Version 1.10, 1993.
[16] E.D. Sehnke, Refractory-grade bauxites: an overview—1993, in: Proceedings of the UNITECR'93, 1993, pp. 658–670.
[17] International Centre for Diffraction Data (ICDD), Powder Diffraction File Database, Newton Square, EE.UU., 1998.
[18] M. Hampel, C.G. Aneziris, Evolution of microstructure and properties of magnesia–carbon refractories during carbonization: effect of grain size and graphite, Ceram. Forum Int. 84 (2007) E125–E131.
[19] J.L. Amorós, V. Beltrán, A. Escardino, M.J. Orts, Permeabilidad al aire de soportes cocidos de pavimento cerámico. La Influencia de las variables de prensado y de la temperatura de cocción, Bol. Soc. Esp. Ceram. Vidr. 31 (1992) 33–38.
[20] A. Conesa, A. Fernandez Roura, J.A. Pitarch, I. Vicente-Mingarro, M.A. Rodriguez, Separation of binary gas mixtures by means of sol–

gel modified ceramic membranes. Prediction of membrane performance, J. Membr. Sci. 155 (1999) 123–131.
[21] B. Rand, B. McEnaney, Carbon binder from polymeric resins and pitch. Part I – pyrolysis behaviour and structure of the carbons, J. Br. Ceram. Trans. 84 (1985) 157–165.
[22] A. Gardziella, J. Suren, M. Belsue, Carbon form phenolic resins: carbon yield and volatile components – recent studies, Interceram 41 (1992) 461–467.
[23] P.O.R.C. Brant, B. Rand, Reactions of silicon and aluminum in MgO–graphite composites: I—Effects on porosity and microestructure, in: Proceedings of the UNITECR´91, 1991, pp. 172–174.
[24] C. Taffin, J. Poirier, The behaviour of metal additives in MgO–C and Al_2O_3–C refractories, Interceram 43 (1994) 354–358 ([5]/458–460 [6]).
[25] C. Baudín, C. Álvarez, R.E. Moore, Influence of chemical reactions in magnesia – graphite refractories I. Effects on texture and high temperature mechanical properties, J. Am. Ceram. Soc. 82 (1999) 3529–3538.
[26] A.S. Gokce, C. Gurcan, S. Ozgen, S. Aydin, The effect of antioxidants on the oxidation behaviour of magnesia–carbon refractory bricks, Ceram. Int. 34 (2008) 323–330.
[27] S. Zhang, N.J. Marriot, W.E. Lee, Thermochemistry and microstructures of MgO–C refractories containing various antioxidants, J. Eur. Ceram. Soc. 21 (2001) 1037–1047.
[28] Z. Nakagawa, N. Enomoto, I. Yi, K. Asano, Effect of corundum/periclase sizes on expansión behavior during synthesis of spinel. in: Proccedings of the UNITECR'95, vol. 1, 1995, pp. 379–386.
[29] S. Migliani, J.J. Uchno, Resin bonded alumina-magnesia–carbon brick for ladles, in: Proccedings of the UNITECR'97, vol. 1, 1997, pp. 193–201.
[30] M. Rigaud, S. Palco, N. Wang, Spinel formation in the MgO–Al_2O_3 system relevant to basic refractories, in: Proceedings of the UNITECR'95, vol. 1, 1995, pp. 387–394.
[31] C.F. Cooper, The role of graphite in the thermal shock resistance of refractories, J. Br. Ceram. Trans. 84 (1985) 57–62.
[32] J.M. Robin, Y. Berthaud, N. Schmitt, J. Poirier, D. Themines, Thermomechanical behaviour of magnesia–carbon refractories, Br. Ceram. Trans. 97 (1998) 1–10.
[33] N. Schmitt, A. Burr, Y. Berthaud, J. Poirier, Micromechanics applied to the thermal shock behavior of refractory ceramics, Mech. Mater. 34 (2002) 725–747.